Space-Time Ambiguity Function for Electronically Scanned ISR

John Swoboda,[1] Joshua Semeter,[1] Philip Erickson[2]

———

Corresponding author: J. P. Swoboda, Department of Electrical & Computer Engineering, Boston University, 8 Saint Marys Street Boston, MA 02215, USA. (swoboj@bu.edu)

[1]Department of Electrical & Computer Engineering, Boston University, Boston, Massachusetts, USA.

[2]Atmospheric Science Division, MIT Haystack Observatory, Westford Massachusetts, USA.

Electronically steerable array (ESA) technology has recently been used in incoherent scatter radars (ISR). These arrays allow for pulse-to-pulse steering of the antenna beam as opposed to a dish antenna which can only measure plasma parameters along one beam at a time. This allows for more flexibility in the measurement of ionospheric plasma parameters.

Currently these systems are operating in the high latitude region where the ionosphere is highly dynamic in both space and time. Because of the highly dynamic nature of the ionosphere in this region it is important to differentiate between artifacts and the true behavior of the plasma. Often the three dimensional data is fitted in a spherical coordinate space and then the parameters are interpolated to a Cartesian grid. This and other sources of error could be impacting the reconstructions of the plasma parameters.

To take advantage of the new flexibility of ESA system we present a new way of analyzing ISR through use of the space-time ambiguity function. This concept is similar to the range ambiguity function that is used in traditional ISR for scanning antenna systems but has been extended to all spatial dimensions along with time as well.

The use of this new ambiguity function allow us to pose this problem in terms of a linear inverse problem for the lags of the intrinsic plasma autocorrelation function. From this we can explore the impact of non-stationarity in the plasma parameters in both time and space. Along with showing possible artifacts we will begin to explore ways of reducing these artifacts.

1. Introduction

Incoherent scatter radar (ISR) is a powerful tool for exploring the ionosphere. These systems can give measurements of electron density N_e, ion temperature T_i, electron temperature T_e, ion velocity V_i and other plasma parameters [*Dougherty and Farley*, 1960; *Farley et al.*, 1961; *Dougherty and Farley*, 1963; *Hagfors*, 1961]. These parameters are measured by fitting a nonlinear theoretic autocorrelation function (ACF) model derived from first principles physics to an estimated time autocorrelation or, alternatively, the power spectrum of the radar signal scattered off of random electron density fluctuations [*Lehtinen and Huuskonen*, 1996].

This is an estimation of a second order statistic of an inherently random process of scattering from electrons. In order to get an estimate of the ACF with reasonable statistical properties numerous pulses have to be averaged together. With traditional dish antennas the ISR system would build these statistics in a limited number of ways. One method consists of pointing the radar beam in a specific direction and hold it there until enough pulses were integrated to get the desired statistics. Alternatively, the beam could be scanned through a field of view and collect pulses while moving. These techniques have an implicit assumption about the uniformity of the plasma parameters within the beam and thus the stationarity of the ACF. The first method assumes a stationarity of the ACF in time while the pulses are collected while the second technique assumes that the velocity of the plasma is known and the beam is scanning along it's velocity or more simply that the plasma parameters, and thus the ACF, are not changing along the motion of the beam.

In many cases, especially in the high latitude ionosphere, this stationarity assumption is not met. Phenomena such as polar cap patches that may be moving through the field of view at very high speeds and may only be with in the beam for a short period of time[*Dahlgren et al.*, 2012a]. Poleward Boundary intensifications also can break these assumptions due to the two dimensional structure [*Zesta et al.*, 2006, 2002].

Recently electronically scannable array (ESA) technology has started to be leveraged by ISR community. The Advance Modular Incoherent Scatter Radar (AMISR) systems have already been deployed both at the Poker Flat Alaska (PFISR) and Resolute Bay Canada (RISR) [ami, 2014]. The EISCAT-3D project is currently being developed using phased array technology as well and will be capable of multistatic processing [eis, 2005]. These new systems are already being used in a number of different ways including creating volumetric reconstructions of plasma parameters [*Semeter et al.*, 2009; *Nicolls and Heinselman*, 2007; *Dahlgren et al.*, 2012a, b].

These new systems differentiate themselves from dish antennas in a fundamental way. Instead of dwelling in a single beam or scanning along a prescribed direction, an ESA can move to a different beam position within its field of view on a pulse by pulse basis. This yields a new flexibility to integrate not only along time but in space in an arbitrary direction. This can help to relax the assumption of stationarity in that now the plasma can move into a different beam and have the returns from the same plasma be integrated together. As opposed to the case with a dish antenna where the returns from different plasma would be improperly averaged together.

68   In order to take advantage of this new flexibility we will put forth the idea of the

69 space-time ambiguity function. This concept extends the range ambiguity to all three

70 spatial dimensions along with time. In the end this ambiguity can be represented as

71 kernel in a Fredholm integral equation,

$$\rho(\mathbf{r}_s) = \int K(\mathbf{r}_s, \mathbf{r}) R(\mathbf{r}) d\mathbf{r} \tag{1}$$

72 where, for ISR, $R(\mathbf{r})$ is the lag of the autocorrelation function at a specific time and

73 position.

74   By using this formulation many parables between ISR and classic camera blurring

75 problems can be made. In cameras blurring can take place when an object moves

76 over a space covered by one pixel while the shutter is open and the CCD is collecting

77 photons. A diagram of this can be seen in Figure 1. The same holds for ISR except

78 that the pixels are no longer square and instead are determined by the beam shape

79 and pulse pattern. This is shown in the diagrams in Figure 2.

80   In this publication we will describe a model for the full space-time ambiguity func-

81 tion for ISR systems. The impact of the three-dimensional ambiguity on moving

82 plasma will be shown through specific cases related to the polar cap patches. A sim-

83 ulation of a polar cap patch using a full ISR simulator, which creates ISR data at

84 the IQ level, will be shown. Lastly possible mitigation techniques will be explored.

85 These mitigation techniques will borrow heavily from the image and signal processing

86 literature.

2. Space-Time Ambiguity

The space-time ambiguity can be thought of as a kernel to a combined volume

and time integration operator. As such definitions of space and time coordinates are

needed.

First a three dimensional coordinate system is defined as $\mathbf{r} = [x, y, z]^T$. For this

coordinate system, $\mathbf{r} = [0, 0, 0]^T$ at the location of the radar and thus $r = |\mathbf{r}|$, also

known as the range variable. This allows for the use of polar coordinates $\mathbf{r} = [r, \theta, \phi]^T$

where θ is the physical elevation angle, ϕ is the physical azimuth angle.

The radar will sample this space into a set of discrete points which will be referred

to as $\mathbf{r}_s = [x_s, y_s, z_s]^T$ along with the discretized range $r_s = |\mathbf{r}_s|$. The sampled

space will consist of a number of points which are the combinations of range gates

and number of beams. These points can also be referred in the polar coordinates

$\mathbf{r}_s = [r_s, \theta_s, \phi_s]^T$, where θ_s is the sampled elevation angle, ϕ_s is the sampled azimuth

angle.

For notation purposes we use two different sets of time commonly known in radar

literature as fast-time, n and slow-time, t [*Richards*, 2005]. Fast-time is used to de-

scribe processes with correlation less then one PRI. Slow-time will used for processes

decorrelate in time on the order of the system's pulse repetition interval (PRI). In

order to form estimates of the ACFs, with desired statistical properties, it is assumed

that the plasma parameters parameters will change on the order of many tens too

hundreds of PRIs. Generally for incoherent scatter the in the E-region of the iono-

107 sphere and above the decorrelation time is less then a PRI, thus the ACFs are formed

108 over fast-time.

109   The terms n and t will represent a continuous variables while n_s and t_s will be

110 the fast time and slow time parameters sampled by the radar. The sampling rate of

111 n_s will be the sampling rate of the A/D converters. The sampling of t_s can at the

112 highest rate, be the PRI and at lowest, sampled once in a non-coherent processing

113 interval (NCPI), or a period of time it takes the radar to average the desired number

114 of pulses.

2.1. Derivation

115   The basic physical mechanism behind ISR is that electron density fluctuations in

116 the ionosphere, $n_e(\mathbf{r}, n)$, scatter radio waves which can be observed by the receiver

117 system of the radar [*Dougherty and Farley*, 1960]. The emitted radar signal at the

118 transmitter will have a pulse shape $s(n)$ modulated at a central frequency that results

119 in a scattering wave number $\mathbf{k}$. Using the Born approximation the signal received at

120 time n, $x(n)$, can be represented as the following

$$x(n) = h(n) * \int e^{-j\mathbf{k}\cdot\mathbf{r}} s\left(n - \frac{2r}{c}\right) n_e(\mathbf{r}, n) d\mathbf{r}, \qquad (2)$$

121 where $h(n)$ is the receiver filter and the $*$ represents the convolution operator. In

122 modern ISR systems this signal $x(n)$ is then sampled at discrete points in fast-time

123 which will be referred to as n_s. The convolution and sampling operation can be

124 brought in the integral as the following,

$$x(n_s) = \int e^{-j\mathbf{k}\cdot\mathbf{r}} s\left(n - \frac{2r}{c}\right) n_e(\mathbf{r}, n) h(n_s - n) d\mathbf{r} dn \tag{3}$$

125   Once the signal has been received and sampled the autocorrelation function is

126   then estimated from the sampled signal $x(n_s)$. The full expression of the underlying

127   autocorrelation of this signal is the following,

$$\langle x(n_s) x^*(n_s')\rangle = \int e^{-j\mathbf{k}\cdot(\mathbf{r}'-\mathbf{r})} s\left(n - \frac{2r}{c}\right) s^*\left(n' - \frac{2r'}{c}\right)$$
$$h(n_s - n) h(n_s' - n') \langle n_e(\mathbf{r}, n) n_e^*(\mathbf{r}', n')\rangle d\mathbf{r} d\mathbf{r}' dn dn', \tag{4}$$

128   where r' is the magnitude of the vector $\mathbf{r}'$. By assuming stationarity of second order

129   signal statistics along fast time, we can then substitute the the lag variables $\tau \equiv n' - n$,

130   and $\tau_s \equiv n_s' - n_s$. With these substitutions Equation 4 becomes

$$\langle x(n_s) x^*(n_s + \tau_s)\rangle = \int e^{-j\mathbf{k}\cdot(\mathbf{r}'-\mathbf{r})} s\left(n - \frac{2r}{c}\right) s^*\left(n + \tau - \frac{2r'}{c}\right)$$
$$h(n_s - n) h(n_s + \tau_s - n - \tau) \langle n_e(\mathbf{r}, n) n_e^*(\mathbf{r}', n + \tau)\rangle d\mathbf{r} d\mathbf{r}' dn d\tau \tag{5}$$

131   We can make a simplifying assumption at this point that the space-time autocorre-

132   lation function of $n_e(\mathbf{r}, t)$, $\langle n_e(\mathbf{r}, n) n_e(\mathbf{r}', n + \tau)\rangle$, will go to zero as the magnitude of

133    $\mathbf{y} \equiv \mathbf{r}' - \mathbf{r}$ increases beyond the debye length[*Farley*, 1969]. The rate that the space-

134   time autocorrelation goes to zero will be such that $\tau \gg \frac{2||\mathbf{y}||}{c}$ thus in the argument of

135   the pulse shape $r \approx r'$. This allows Equation 5 to be rewritten as

$$\langle x(n_s)x^*(n_s+\tau)\rangle = \int s\left(n-\frac{2r}{c}\right)s^*\left(n+\tau-\frac{2r}{c}\right)h(n_s-n)h^*(n_s+\tau_s-n-\tau)$$
$$\left[\int e^{-2j\mathbf{k}\cdot\mathbf{y}}\langle n_e(\mathbf{r},n)n_e^*(\mathbf{y}+\mathbf{r},n+\tau)\rangle d\mathbf{y}\right]d\mathbf{r}dnd\tau. \quad (6)$$

The inner integral is a spatial Fourier transform evaluated at the wave number of the radar $\mathbf{k}$. By again asserting stationarity along slow time we can represent the true ACF as the following,

$$R(\tau,\mathbf{r}) = \langle|n_e(\mathbf{k},r,\tau)|^2\rangle \equiv \int e^{-2j\mathbf{k}\cdot\mathbf{y}}\langle n_e(\mathbf{r},b)n_e^*(\mathbf{y}+\mathbf{r},n+\tau)\rangle d\mathbf{y}. \quad (7)$$

Now Equation 6 becomes

$$\langle x(n_s)x^*(n_s+\tau_s)\rangle = \int \langle|n_e(\tau,\mathbf{k},\mathbf{r})|^2\rangle\left[\int s(n-\frac{2r}{c})s^*(n+\tau-\frac{2r}{c})h(n_s-n)h^*(n_s+\tau_s-n-\tau)dn\right]d\tau dr. \quad (8)$$

If n_s is replaced with $2r_s/c$ we can introduce the range ambiguity function $W(\tau_s,r_s,\tau,r)$ by doing the following substitution,

$$W(\tau_s,r_s,\tau,r) = \int s(n-\frac{2r}{c})s^*(n+\tau-\frac{2r}{c})h(2r_s/c-n)h^*(2r_s/c+\tau_s-n-\tau)dn. \quad (9)$$

Assuming, for the moment, that $R(\tau,\mathbf{r})$ only varies across the range dimension r we can now represent this in the form of a Fredholm integral equation

$$\langle x(2r_s/c)x^*(2r_s/c+\tau_s)\rangle = \int W(\tau_s,r_s,\tau,r)R(\tau,r)drd\tau. \quad (10)$$

The range ambiguity function, $W(\tau_s,r_s,\tau,r)$, can be thought of as a smoothing operator along the range and lag dimensions of $R(\tau,r)$.

The spatial ambiguity across angle is determined by the antenna beam pattern. In phase array radars this beam pattern is ideally the array factor multiplied by the element pattern [*Balanis*, 2005]. The array factor is determined by a number of things including the element spacing in both x and y (dx, dy) and the wave number of the radar, k. Making idealized assumptions with no mutual coupling and that the array elements are cross dipole elements AMISR systems will have the following antenna pattern for pointing angle (θ_s, ϕ_s),

$$F(\theta_s, \phi_s, \theta, \phi) = \frac{1}{2}(1+\cos(\theta)^2)\left[\frac{1}{MN}\left(1 + e^{j(\psi_y/2+\psi_x)}\right)\frac{\sin((M/2)\psi_x)}{\sin(\psi_x)}\frac{\sin((N/2)\psi_x)}{\sin(\psi_x/2)}\right]^2,$$

(11)

where $\psi_x = -kd_x(\sin\theta\cos\phi - \sin\theta_s\cos\phi_s)$, $\psi_y = -kd_y(\sin\theta\sin\phi - \sin\theta_s\sin\phi_s)$ and M is the number of elements in the x direction of the array, and N is the number of elements in the y direction(see Appendix: A for derivation).

The spatial ambiguity is a separable function made up of the components of $W(\tau_s, \tau, r_s, r)$ and $F(\theta_s, \phi_s, \theta, \phi)$. These two functions can be combined by multiplying the two, creating the spatial ambiguity function $K(\tau_s, \mathbf{r}_s, \tau, \mathbf{r})$, and then doing a volume integration. This will create radar system's estimate of the ACF using one pulse which will be referred to as $\rho(\tau_s, \mathbf{r}_s)$,

$$\rho(\tau_s, \mathbf{r}_s) = \int F(\theta_s, \phi_s, \theta, \phi)W(\tau_s, r_s, \tau, r)R(\tau, \mathbf{r})dV, \qquad (12)$$

$$= \int K(\tau_s, \mathbf{r}_s, \tau, \mathbf{r})R(\tau, \mathbf{r})dV. \qquad (13)$$

149 A rendering of an example of this full ambiguity function for an uncoded long pulse

150 and antenna pattern in Equation 11 for four beams can be seen in Figure 3.

151 This one pulse is a single sample of a random process. In order to create a usable

152 estimate multiple samples of this ACF need to be averaged together to reduce the

153 variance to sufficient levels in order to fit the estimate to a theoretical ACF that is

154 tied to plasma parameter values. To show the impact of this averaging to create the

155 estimate of the ACF we will add slow-time dependence to $R(\tau, \mathbf{r}, t)$ along with another

156 separable function $G(t_s, t)$ to the kernel. This function $G(t_s, t)$, while reducing the

157 variance can create blurring of the ACF if the plasma parameters change with in a

158 NCPI. Since the radar is sampling the space with individual pulses this function can

159 take the form of a summation of Dirac delta functions

$$G(t_s, t) = \sum_{j=0}^{J-1} \alpha_j \delta(t - t_s - jT_{PRI}), \tag{14}$$

160 where J is the number of pulses used over a NCPI, T_{PRI} is the PRI time period and

161 α_j is the weights that the radar assigns to the pulses. The weights are generally set

162 to $1/J$ to simply average the pulses. With Equation 14 incorporated into the overall

163 ambiguity we see the full integral equation,

$$\rho(\tau_s, \mathbf{r}_s, t_s) = \int G(t_s, t) K(\tau_s, \mathbf{r}_s, \tau, \mathbf{r}) R(\tau, \mathbf{r}, t) dV dt \tag{15}$$

$$\rho(\tau_s, \mathbf{r}_s, t_s) = \int L(\tau_s, \mathbf{r}_s, t_s, \tau, \mathbf{r}, t) R(\tau, \mathbf{r}, t) dV dt. \tag{16}$$

164 The final kernel, $L(\tau_s, \mathbf{r}_s, t_s, \tau, \mathbf{r}, t)$ encompasses the full space-time ambiguity.

2.2. Ambiguity after Frame Transformation

165   We will now focus on the impact of the motion of plasma as it is going through

166   the field of view of the radar. We will assume that the radar is integrating over a

167   length of time T beginning at t_s. The kernel L will be represented as a separable

168   function K and G as in Equation 15. In this case G will be a summation of Dirac

169   delta functions with weights of $1/J$. This will change Equation 15 to the following,

$$\rho(\tau_s, \mathbf{r}_s, t_s) = \int K(\tau_s, \mathbf{r}_s, \tau, \mathbf{r}) \left[(1/J) \int_{t_s}^{t_s+T} \sum_{j=0}^{J-1} \delta(t - t_s - jT_{PRI}) R(\tau, \mathbf{r}, t) dt \right] dV. \tag{17}$$

170   Of specific interest are instances in the high latitude ionosphere where embedded

171   plasma structures are moving due to the electric field of the magnetosphere. Because

172   of this it will be assumed that the plasma is a rigid object and will not deform with

173   respect to $\mathbf{r}$ over time period $[t_0, t_0 + T]$ where $T = JT_{PRI}$ is the time for one NCPI.

174   Also it will be assumed that it will be moving with a constant velocity $\mathbf{v}$. Thus

175    $R(\tau, \mathbf{r}, t) \Rightarrow R(\tau, \mathbf{r} + \mathbf{v}t)$. The assumption of rigidity is possible to make over the

176   time period of the NCPI, on the order of a few minutes, while the plasma moves

177   through the field of view of the radar. One example can be taken from the high

178   latitude ionosphere while large scale features in structures such as patches decay on

179   the order of hours[*Tsunoda*, 1988]. This assumption is useful because it shows the

180   utility of this frame work to analyze the impacts on the true resolution of the ISR

181   systems. With these assumption Equation 17 becomes,

$$\rho(\tau_s, \mathbf{r}_s, t_s) = (1/J) \int \int_{t_s}^{t_s+T} \sum_{j=0}^{J-1} \delta(t - t_s - jT_{PRI}) K(\tau_s, \mathbf{r}_s, \tau, \mathbf{r}) R(\tau, \mathbf{r} + \mathbf{v}t) dt dV \quad (18)$$

A change of variables to $\mathbf{r}' = \mathbf{r} + \mathbf{v}t$ acts as a Galilean transform and applies a warping to the kernel, changing the frame of reference. Since $R(\tau, \mathbf{r}')$ is no longer dependent on t Equation 18 becomes,

$$\rho(\tau_s, \mathbf{r}_s, t_s) = (1/J) \int \left[\sum_{j=0}^{J-1} K(\tau_s, \mathbf{r}_s, \tau, \mathbf{r}' - \mathbf{v}(t_s + jT_{PRI})) \right] R(\tau, \mathbf{r}') dV. \quad (19)$$

By performing the integration in t the problem can now be simplified further back to a Fredholm integral equation by simply replacing the terms in the square brackets as a new kernel $A(\tau_s, \mathbf{r}_s, t_s, \tau, \mathbf{r}')$,

$$\rho(\tau_s, \mathbf{r}_s, t_s) = \int A(\tau_s, \mathbf{r}_s, t_s, \tau, \mathbf{r}') R(\tau, \mathbf{r}') dV. \quad (20)$$

The impact of the plasma velocity on the ambiguity function can be seen in Figure 4. This is the same ambiguity as seen in Figure 3 but with a velocity of 500 m/s in the y direction over a period of 2 minutes. This velocity creates a larger ambiguity function in the frame of reference of the moving plasma.

The operator A can be determined through knowledge of the radar system's beam pattern along with the experiments pulse pattern, integration time and velocity of the plasma. This velocity $\mathbf{v}$ can be estimated by taking measurements of the Doppler shift and using a methodology seen in [*Butler et al.*, 2010]. Once the operator has

196 been determined standard processing techniques can be used as if the plasma is not

197 moving, under the previous assumptions.

3. Simulation

198 Although Figures 3 and 4 show the spatial extent of the space-time ambiguity func-

199 tion both with and without target motion, the impact of this on the reconstruction

200 data can better shown through simulation. To do so we show data from a 3-D ISR

201 simulator with a known ionosphere. In the following section we describe this simu-

202 lator along with two case studies to show the impact of this ambiguity on properly

203 reconstructing the parameters in the ionosphere.

3.1. Simulator

204 The simulator creates data by deriving time filters from the autocorrelation function

205 and applying them to complex white Gaussian noise generators. Stating this in

206 another way, every point in time and space has a noise plant and filter structure as

207 in Figure 5. The data is then scaled and summed together according to its location

208 in range and angle space to radar.

209 After the IQ data has been created it is processed to create estimates of the ACF

210 at desired points of space. This processing a follows flow chart seen in Figure 6.

211 The sampled I/Q can be represented as $x(n) \in \mathbb{C}^N$ where N is the number of

212 samples in an inter pulse period. At this point the first step in estimating the auto-

213 correlation function is taken. For each range gate $m \in 0, 1, ...M-1$ an autocorrelation

214 is estimated for each lag of $l \in 0, 1..., L-1$. This operation of forming the ACF esti-

215   mates repeats for each pulse, $j \in 0, 1, ...J - 1$, and is then summed over the J pulses.

216   The entire operation to form the initial estimate of $\hat{R}(m, l)$ is the following,

$$\hat{R}(m, l) = \sum_{j=0}^{J-1} x(m - \lfloor l/2 \rfloor, j) x^*(m + \lceil l/2 \rceil, j). \tag{21}$$

217   The case shown in Equation 21 is a centered lag product, other types of lag product

218   calculations are available but generally a centered product is used. In the centered lag

219   product case range gate index m and sample index n can be related by $m = n - \lfloor L/2 \rfloor$

220   and the maximum lag and sample relation is $M = N - \lceil L/2 \rceil$.

221   After the lag products have been formed an estimate of the noise correlation is

222   subtracted out of $\hat{R}(m, l)$, which is defined as $\hat{R}_w(m, l)$,

$$\hat{R}_w(m_w, l) = \sum_{j=0}^{J-1} w(m_w - \lfloor l/2 \rfloor, j) w^*(m_w + \lceil l/2 \rceil, j), \tag{22}$$

223   where $w(n_w)$ is the background noise process of the radar. Often the noise process is

224   sampled during a calibration period for the radar when nothing is being emitted.

225   The final estimate of the autocorrelation function after the noise subtraction and

226   summation rule will be represented by $\hat{R}_f(m, l)$. At this point a summation rule is

227   applied and the data is sent off to be fit. The final parameters are derived through a

228   standard Levenberg-Marquart non-linear least-squares fitting of n_e, T_i, T_e [*Levenberg,*

229   *1944*].[1]

3.2. Case 1

²³⁰ The first example is a simple case of a small plasma enhancement moving through

²³¹ the radar field of view. This case is meant to model conditions expected in the

²³² polar cap ionosphere under southward IMF conditions [*Dahlgren et al.*, 2012b]. The

²³³ background electron density varies in altitude as a Chapman function, shown in

²³⁴ Figure 7, while the electron and ion temperature remains constant.

²³⁵ Embedded in the background there is a 35 km radius sphere of enhanced electron

²³⁶ density of 5×10^{10} m^{-3} centered at 400 km altitude moving at 500 m/s along the

²³⁷ **y** direction. Images from this phantom can be seen in Figure 8. For the ease of

²³⁸ comparison the phantom is only shown in areas where its in the radar's field of view.

²³⁹ The positions of the 121 beam used for this case can be seen in Figure 9.

²⁴⁰ Because only the electron density is varying the fitting method becomes simply a

²⁴¹ power estimate as the electron density is directly proportional to the return power if

²⁴² the temperature ration is known. This example allows the blurring from the space-

²⁴³ time ambiguity function can be observed easier, while also showing trade offs between

²⁴⁴ statistical variance and blurring. [2]

²⁴⁵ Using the phantom we can see how just simply changing the integration time can

²⁴⁶ impact the reconstruction. In Figure 10 we can see a case were only 10 pulses are used

²⁴⁷ for the reconstruction,which corresponds to an integration time of about 9 seconds.

²⁴⁸ The enhancement can be seen as it moves through the field of view although there

²⁴⁹ is that there is a high amount of variance in the reconstruction. Figure 11 shows

²⁵⁰ the reconstruction with 200 pulses, 3 minute integration time. The variability has

251 been reduced but there is a large amount of blurring of the enhancement as it moves

252 through the field of view.

253 In order to give a comparison a phantom was also created one with no motion.

254 This can be seen in first pane Figure 12. An image using the same integration time

255 as in Figure 10 for the stationary phantom is the center pane in Figure 12. Another

256 image using the longer integration time can be seen in right pane of Figure 12. These

257 images show that the blurring is on the same order between both integration times.

3.3. Case 2

258 Lastly, we show results of a simulation of the plasma density enhancement through

259 the field of view but the ion and electron temperatures are allowed to vary. We

260 again use a plasma enhancement moving through the field of view at 500 m/s but

261 the electron and ion temperature varies with time and altitude. The the background

262 ion and electron temperature vs. height can be seen in Figure 14. As the electron

263 density enhancement travels through the field of view the temperatures drop by the

264 same ratio that the electron density is enhanced. This is done to keep the variance

265 the same.

266 The phantoms for each parameter at approximately 402 seconds can be seen in

267 Figure 14. The reconstruction of this field at the same time can be seen in Figure 15.

268 The reconstruction does not seem to show the electron density enhancement even in

269 a blurred form. This is likely due to the nonlinear nature of the fitting.

4. Possible Mitigation Techniques

²⁷⁰   There are a number of possible ways to remove the ISR operator function to the

²⁷¹ data. A relatively simply way to remove the problem is to process the data in the

²⁷² frame of reference of the plasma. Already it has been shown that it is possible to

²⁷³ measure the vector velocity of plasma flows, [*Butler et al.*, 2010]. After measuring the

²⁷⁴ velocity instead of integrating in the same beam one could integrate across different

²⁷⁵ beams using this knowledge. This would allow for ACF to be formed from the same

²⁷⁶ populations of plasma as it moves through the field of view.

²⁷⁷   In order to reconstruct the plasma parameters it is necessary to do some sort

²⁷⁸ of regularization. There are two type of regularization that can be applied in this

²⁷⁹ case the first is parameter based regularization, like full profile analysis *Holt et al.*

²⁸⁰ [1992]; *Hysell et al.* [2008]. The term parameter based regularization in this case

²⁸¹ means applying constraints to the physical parameters that are often determined

²⁸² after fitting. This requires a large amount of calculation because the fitting and

²⁸³ constraints are done in one step. Currently full profile analysis has only been applied

²⁸⁴ along the range dimension and not in all three spatial dimensions.

²⁸⁵   The other method will be referred to as data based regularization. This term

²⁸⁶ infers the application of constraints to the estimates of the autocorrelation functions.

²⁸⁷ The constraints usually deal with how the data changes over time and space by

²⁸⁸ constraining the energy of the ACFs or its derivative. This has an advantage of

²⁸⁹ being more computationally tractable in that it is now a linear inverse problem.

²⁹⁰ Using the ideas stated in this paper one can cast the reconstruction of the four

dimensional function of the ACFs in these terms. The issue with doing this data based reconstruction is it is unknown how to constrain the reconstruction in the best way.

The two examples of data based regularization in the one dimensions ISR literature are lag profile inversion and deconvolution methods. Lag profile inversion creates an operator that takes the measured data from a theoretical ACFs to the measured ACFs [*Virtanen et al.*, 2008]. Along with the operator there is also an assumed Gaussian error. This error can be then estimated from the data. This Bayesian frame work can actually be rewritten as a least squares minimization along with a Tikhonov constraint. Because of this one can show that the deconvolution methods from *Nikoukar et al.* [2008] are extremely similar to lag profile inversion with differences in only what type of constraints are used.

In order to properly process data from ESA systems these methods will have to be extended to all three dimensions. Both methods have advantages and disadvantages. In data based regularization constraints must be applied to the ACFs, which yields the question of what is the most reasonable constraint to use. Although this methodology will allow researchers to use methods from linear inverse theory, which has been well studied. The parameter based regularization method allows for use of physics based constraints to reconstruct the parameters. This technique though would likely yield solutions that would be very computationally intensive compared to techniques for data based regularization. In any case, both methods requires the forward model which has been discussed in this paper.

5. Conclusion

{313} We have presented a new method for analyzing incoherent scatter radar processing

{314} through use of the full space-time ambiguity function. This allows for taking into

{315} account the antenna beam pattern, pulse pattern and time integration. Through

{316} simulation we have shown how plasma motion can impact reconstruction of parame-

{317} ters which compounded with the non-linear nature of the parameter fitting step can

{318} create errors which are hard to predict. Lastly we have suggested a number of ways

{319} using three dimensional ISR systems we could mitigate these errors and reconstruct

{320} parameters at higher resolutions then what is currently possible.

Appendix A: Derivation of Idealized AMISR Array Pattern

{321} The current antenna on the AMISR systems is made up 8x16 set of panel of half

{322} wave cross dipoles. Each panel has 32 cross dipoles in a 8x4 hexagonal configuration.

{323} In the current set up at the Poker Flat site this yields at 4096 element array in a

{324} 64x64 element hexagonal configuration.

{325} In order to simplify the antenna can be treated as two rectangular arrays of cross

{326} dipoles interleaved together. In the x direction each of these arrays will have a spacing

{327} of $2d_x$ with $M/2$ elements. The y direction will be of length N elements and spacing

{328} d_y. Using basic planar phase array theory, [$Balanis$, 2005], we can start with the

{329} linear array pattern from the first array can be represented as

$$E_1(\theta, \phi) = \sum_{m=1}^{M/2} \sum_{n=1}^{N} e^{-j2(m-1)kd_x \sin\theta\cos\phi - j(n-1)kd_y \sin\theta\sin\phi}. \tag{A1}$$

330   Since the second array can be though of a shifted version of the first in the x direction

331   we get the following

$$E_2(\theta, \phi) = \sum_{m=1}^{M/2} \sum_{n=1}^{N} e^{-j(2m-1)kd_x \sin\theta\cos\phi - j(n-1/2)kd_y \sin\theta\sin\phi}. \qquad (A2)$$

332   In order to simplify notation we will make the following substitutions, $\psi_x =$

333   $-kd_x \sin\theta\cos\phi$, $\psi_y = -kd_y \sin\theta\sin\phi$. Using Equations A1 and A2 we can see the

334   following relationship,

$$E_2(\theta, \phi) = e^{j(\psi_y/2 + \psi_x)} E_1(\theta, \phi) = \sum_{m=1}^{M/2} \sum_{n=1}^{N} e^{-j2(m-1)\psi_x - j(n-1)\psi_y}. \qquad (A3)$$

335   Adding E_1 and E_2 together we get the following linear array pattern

$$E(\theta, \phi) = \left(1 + e^{j(\psi_y/2 + \psi_x)}\right) \sum_{m=1}^{M/2} \sum_{n=1}^{N} e^{-j2(m-1)\psi_x - j(n-1)\psi_y}.$$
$$= \frac{1}{MN} \left(1 + e^{j(\psi_y/2 + \psi_x)}\right) \frac{\sin((M/2)\psi_x)}{\sin(\psi_x)} \frac{\sin((N/2)\psi_x)}{\sin(\psi_x/2)}. \qquad (A4)$$

336   Since the array is steerable this can be taken into account in the equations by

337   simply changing the definitions of ψ_x and ψ_y to $\psi_x = kd_x(\sin\theta\cos\phi - \sin\theta_s\cos\phi_s)$,

338   and $\psi_y = kd_y(\sin\theta\sin\phi - \sin\theta_s\sin\phi_s)$. Lastly the antenna pattern of a single cross

339   dipole can be represented as $\frac{1}{2}(1 + \cos^2(\theta))$[*Balanis*, 2005]. By taking the squared

340   magnitude of the array factor and multiplying it with the pattern of the dipole we

341   get Equation 11,

$$F(\theta_s, \phi_s, \theta, \phi) = \frac{1}{2}(1 + \cos(\theta)^2) \left| \frac{1}{MN} \left(1 + e^{j(\psi_y/2+\psi_x)}\right) \frac{\sin((M/2)\psi_x)}{\sin(\psi_x)} \frac{\sin((N/2)\psi_x)}{\sin(\psi_x/2)} \right|^2.$$

(A5)

Notes

1. I just checked my code and it seems that I did not use V_i in my fitting. If this needs to be redone please let me know.

342

2. I think we had a better way of stating this.

References

343   (2005), Eiscat 3d design specification document.

344   (2014), Amisr overview.

345   Balanis, C. A. (2005), *Antenna Theory: Analysis and Design*, Wiley-Interscience.

346   Butler, T. W., J. Semeter, C. J. Heinselman, and M. J. Nicolls (2010), Imaging f

347   region drifts using monostatic phased-array incoherent scatter radar, *Radio Sci.*,

348   *45*(5), RS5013, doi:10.1029/2010RS004364.

349   Dahlgren, H., J. L. Semeter, K. Hosokawa, M. J. Nicolls, T. W. Butler, M. G. Johnsen,

350   K. Shiokawa, and C. Heinselman (2012a), Direct three-dimensional imaging of polar

351   ionospheric structures with the resolute bay incoherent scatter radar, *Geophysical*

352   *Research Letters*, *39*(5), n/a–n/a, doi:10.1029/2012GL050895.

353   Dahlgren, H., G. W. Perry, J. L. Semeter, J. P. St. Maurice, K. Hosokawa,

354   M. J. Nicolls, M. Greffen, K. Shiokawa, and C. Heinselman (2012b), Space-

355   time variability of polar cap patches: Direct evidence for internal plasma struc-

turing, *Journal of Geophysical Research: Space Physics*, *117*(A9), A09,312, doi: 10.1029/2012JA017961.

Dougherty, J. P., and D. T. Farley (1960), A theory of incoherent scattering of radio waves by a plasma, *Proceedings of the Royal Society of London. Series A, Mathematical and Physical Sciences*, *259*(1296), pp. 79–99.

Dougherty, J. P., and D. T. Farley (1963), A theory of incoherent scattering of radio waves by a plasma, 3 scattering in a partly ionized gas, *Journal of Geophysical Research*, *68*, 5473.

Farley, D. T. (1969), Incoherent scatter correlation function measurements, *Radio Sci.*, *4*(10), 935–953.

Farley, D. T., J. P. Dougherty, and D. W. Barron (1961), A theory of incoherent scattering of radio waves by a plasma ii. scattering in a magnetic field, *Proceedings of the Royal Society of London. Series A, Mathematical and Physical Sciences*, *263*(1313), pp. 238–258.

Hagfors, T. (1961), Density fluctuations in a plasma in a magnetic field, with applications to the ionosphere, *Journal of Geophysical Research*, *66*(6), 1699–1712, doi:10.1029/JZ066i006p01699.

Holt, J. M., D. A. Rhoda, D. Tetenbaum, and A. P. van Eyken (1992), Optimal analysis of incoherent scatter radar data, *Radio Science*, *27*(3), 435–447, doi: 10.1029/91RS02922.

Hysell, D. L., F. S. Rodrigues, J. L. Chau, and J. D. Huba (2008), Full profile incoherent scatter analysis at jicamarca, *Annales Geophysicae*, *26*(1), 59–75, doi:

378   10.5194/angeo-26-59-2008.

379 Lehtinen, M. S., and A. Huuskonen (1996), General incoherent scatter analysis

380   and {GUISDAP}, *Journal of Atmospheric and Terrestrial Physics*, *58*(1–4), 435

381   – 452, doi:http://dx.doi.org/10.1016/0021-9169(95)00047-X, ¡ce:title¿Selected pa-

382   pers from the sixth international Eiscat Workshop¡/ce:title¿.

383 Levenberg, K. (1944), A method for the solution of certain non-linear problems in

384   least squares, *Quarterly of Applied Mathematics*, *2*, 164–168.

385 Nicolls, M. J., and C. J. Heinselman (2007), Three-dimensional measurements of

386   traveling ionospheric disturbances with the Poker Flat Incoherent Scatter Radar,

387   *Geophysical Research Letters*.

388 Nikoukar, R., F. Kamalabadi, E. Kudeki, and M. Sulzer (2008), An efficient near-

389   optimal approach to incoherent scatter radar parameter estimation, *Radio Science*,

390   *43*(5), n/a–n/a, doi:10.1029/2007RS003724.

391 Richards, M. A. (2005), *Fundamentals of Radar Signal Processing*, McGraw-Hill.

392 Semeter, J., T. Butler, C. Heinselman, M. Nicolls, J. Kelly, and D. Hamp-

393   ton (2009), Volumetric imaging of the auroral ionosphere: Initial results from

394   pfisr, *Journal of Atmospheric and Solar-Terrestrial Physics*, *71*, 738 – 743, doi:

395   10.1016/j.jastp.2008.08.014, ¡ce:title¿Advances in high latitude upper atmospheric

396   science with the Poker Flat Incoherent Scatter Radar (PFISR)¡/ce:title¿.

397 Tsunoda, R. T. (1988), High-latitude F region irregularities: A review and synthesis,

398   *Reviews of Geophysics*.

399 Virtanen, I. I., M. S. Lehtinen, and T. Nygrén (2008), Lag profile inversion method

400   for EISCAT data analysis, *Annales . . . .*

401 Zesta, E., E. Donovan, L. Lyons, G. Enno, J. S. Murphree, and L. Cogger (2002),

402   Two-dimensional structure of auroral poleward boundary intensifications, *Jour-*

403   *nal of Geophysical Research: Space Physics*, *107*(A11), SIA 6–1–SIA 6–20, doi:

404   10.1029/2001JA000260.

405 Zesta, E., L. Lyons, C.-P. Wang, E. Donovan, H. Frey, and T. Nagai (2006), Auroral

406   poleward boundary intensifications (pbis): Their two-dimensional structure and

407   associated dynamics in the plasma sheet, *Journal of Geophysical Research: Space*

408   *Physics*, *111*(A5), n/a–n/a, doi:10.1029/2004JA010640.

(a) CCD No Blur   (b) CCD With Blur

Figure 1.   CCD camera

(a) Radar No Blur   (b) Radar With Blur
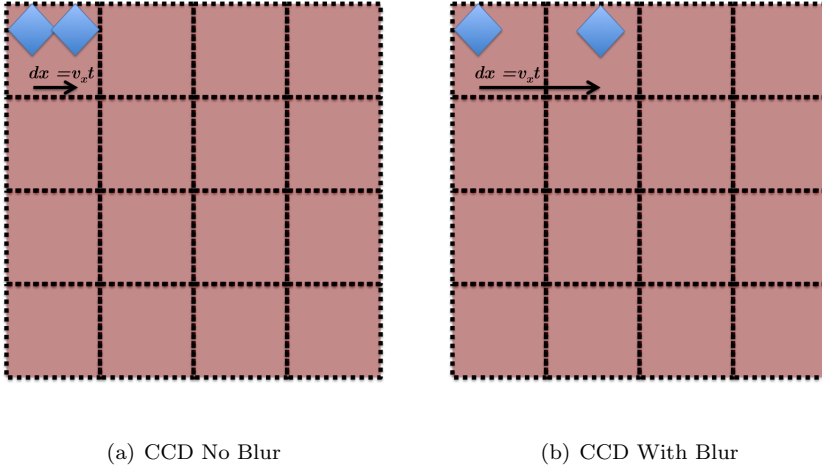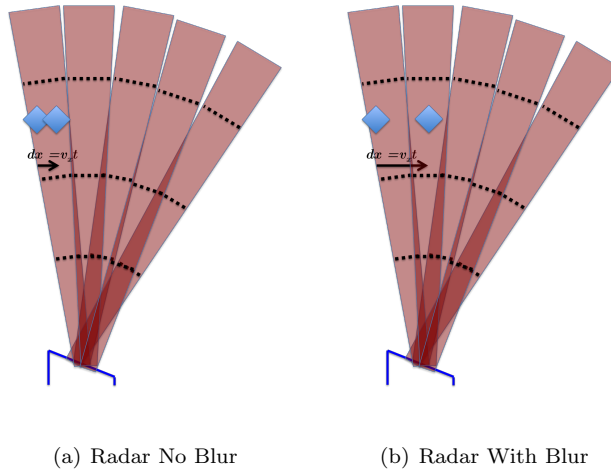
Figure 2.   Radar
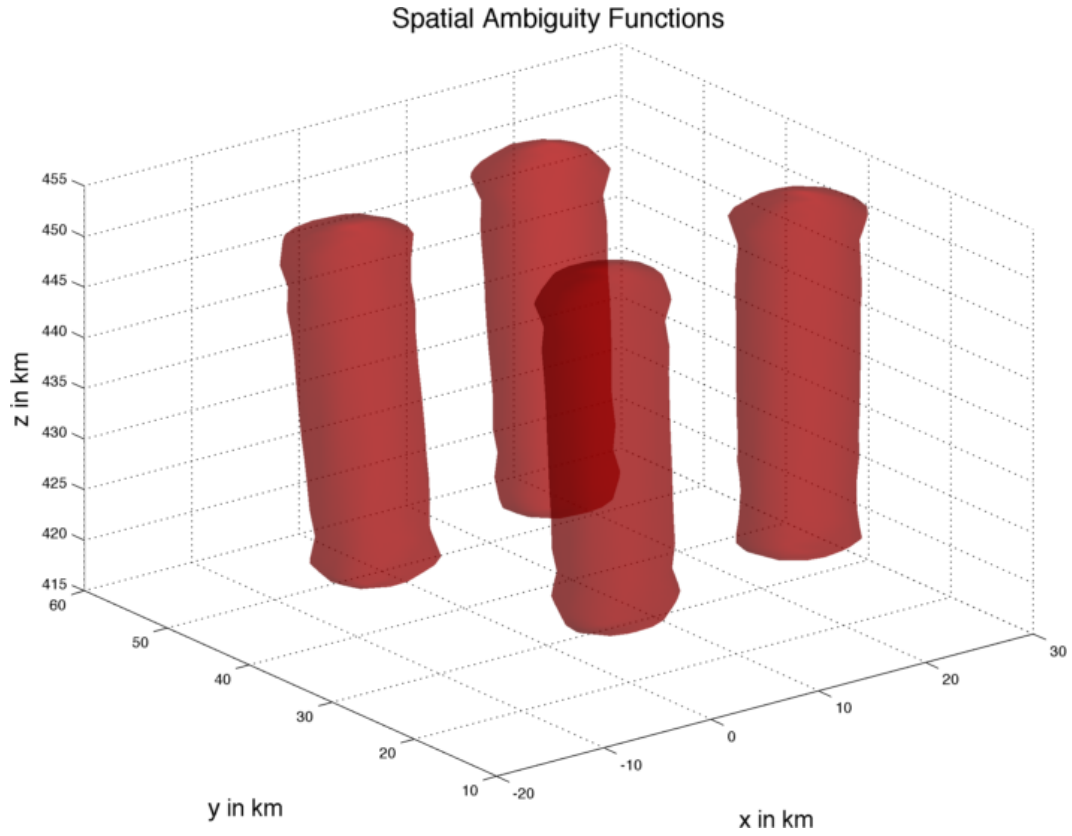
Figure 3. Full Spatial Ambiguity Function
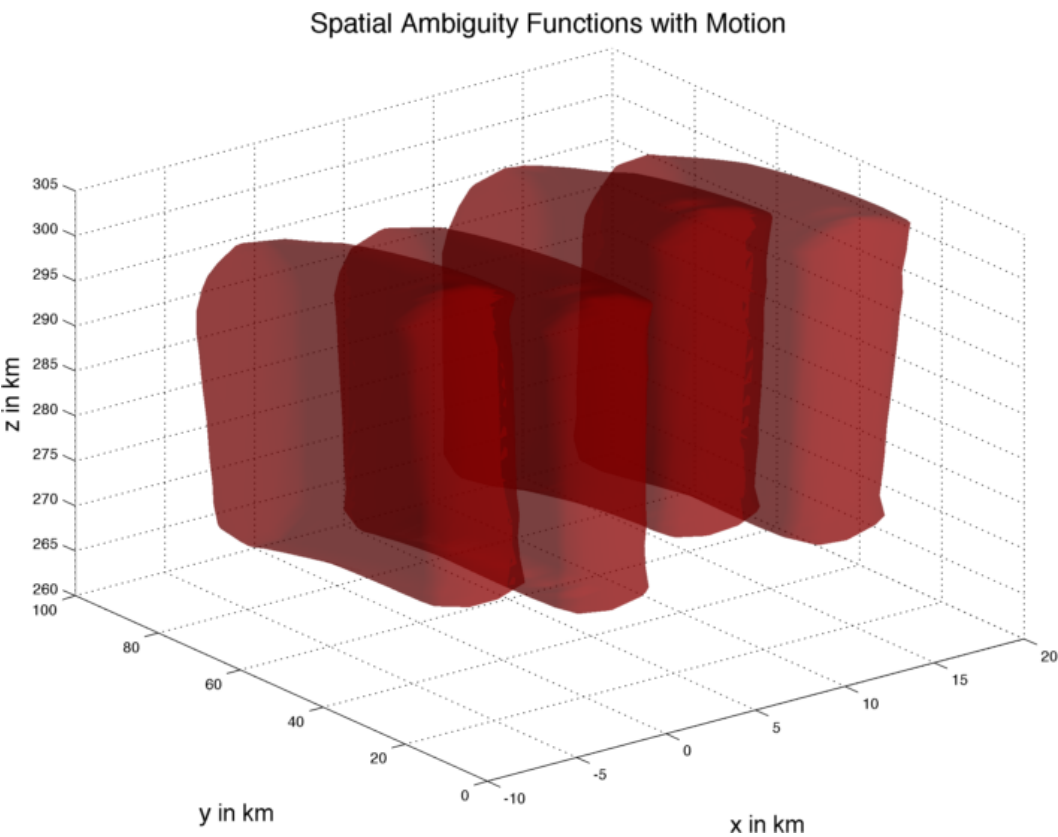
Figure 4.   Full Spatial Ambiguity Function With Motion
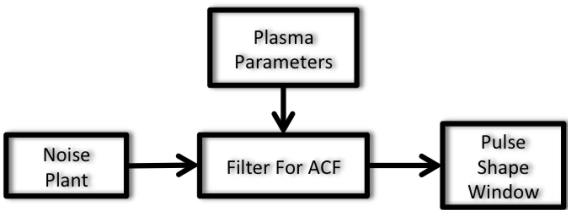
Figure 5.   I/Q Simulator Diagram
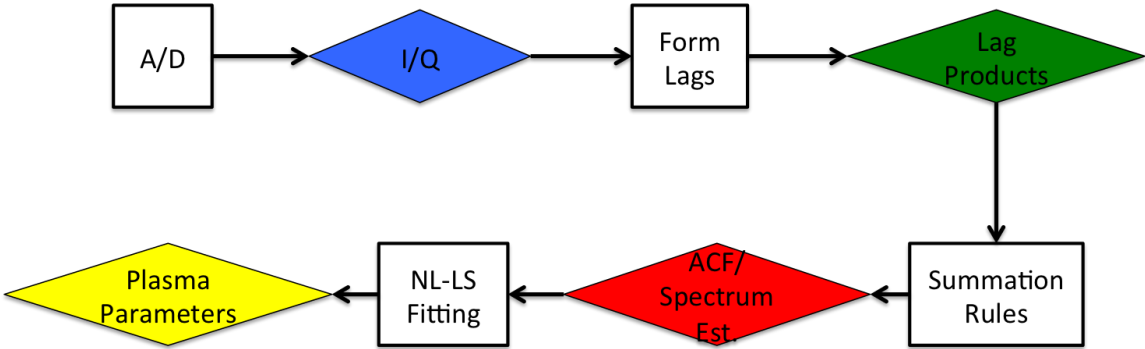
Figure 6. ISR Processing Chain.
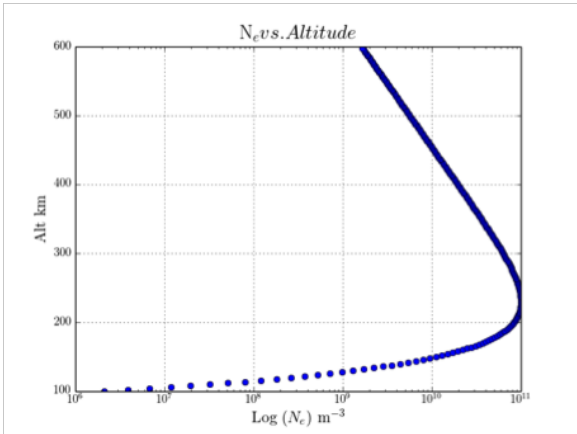
Figure 7. Electron Density vs. Altitude.
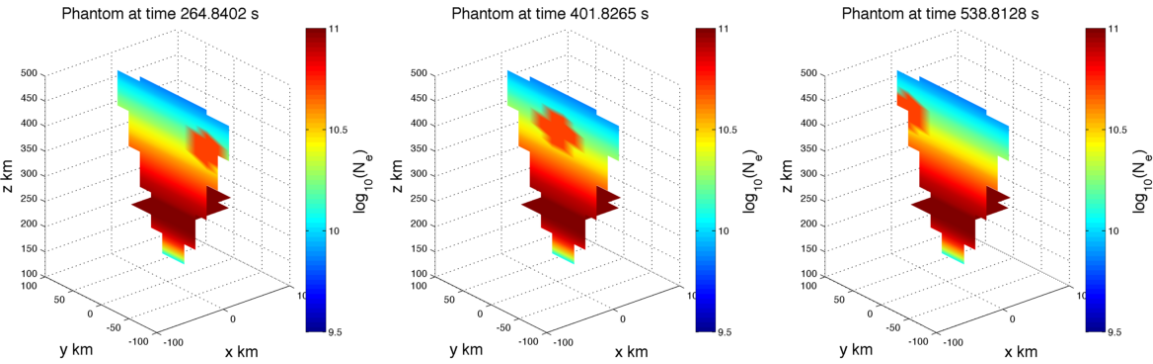
Figure 8.   Images from Phantom.
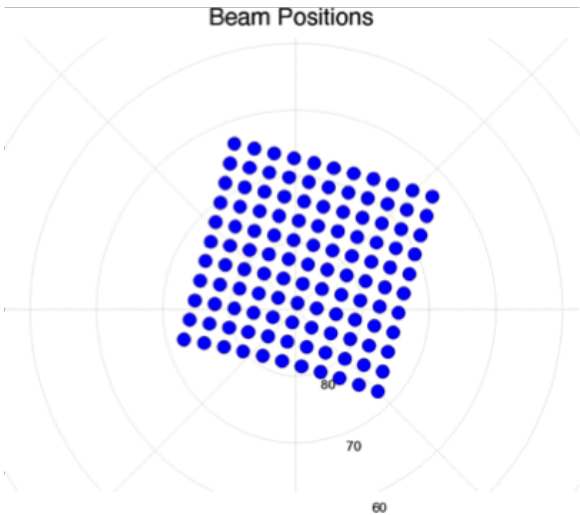
Figure 9.   Beam Pattern
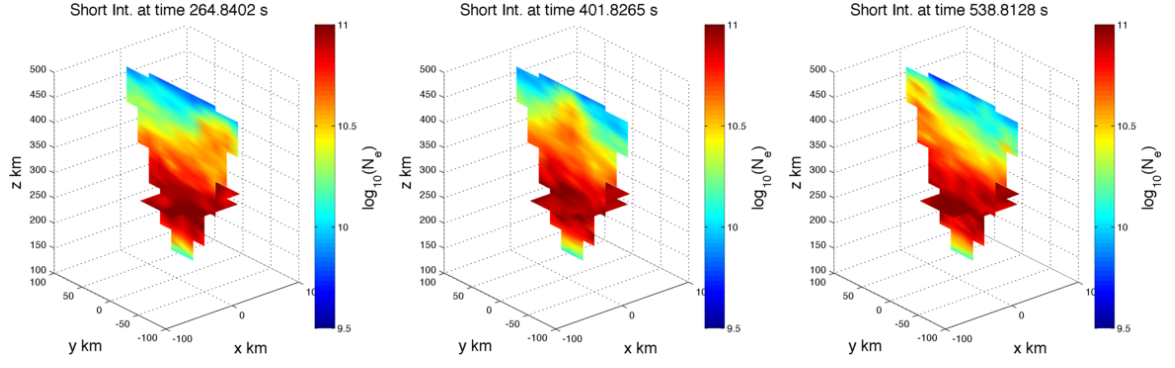
Figure 10. Images from Reconstruction Using Only 10 Pulses.
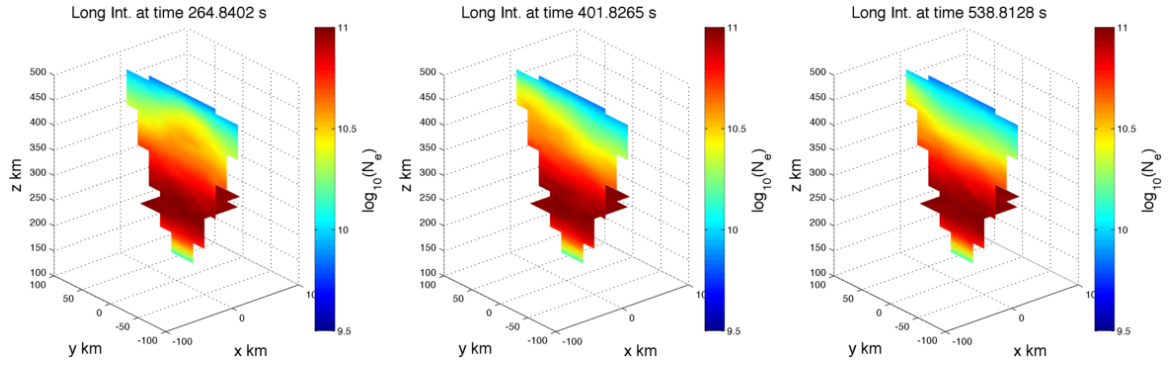
Figure 11. Images from Reconstruction Using 200 Pulses.
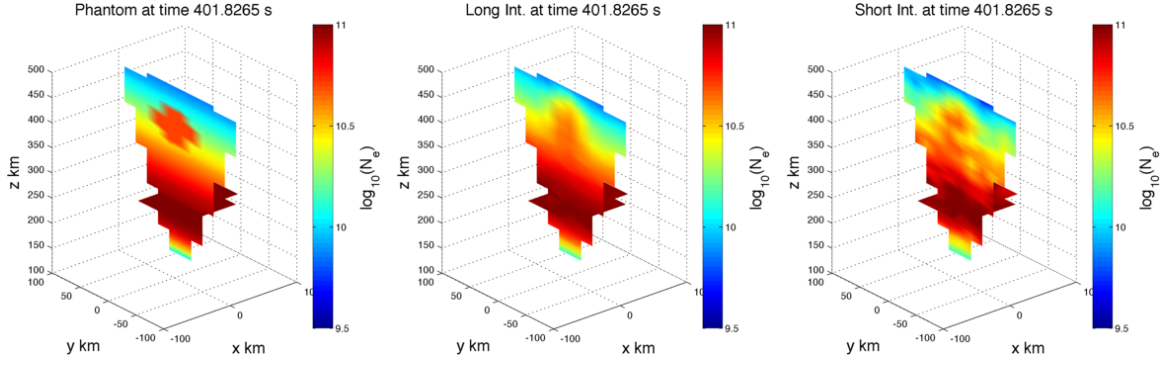
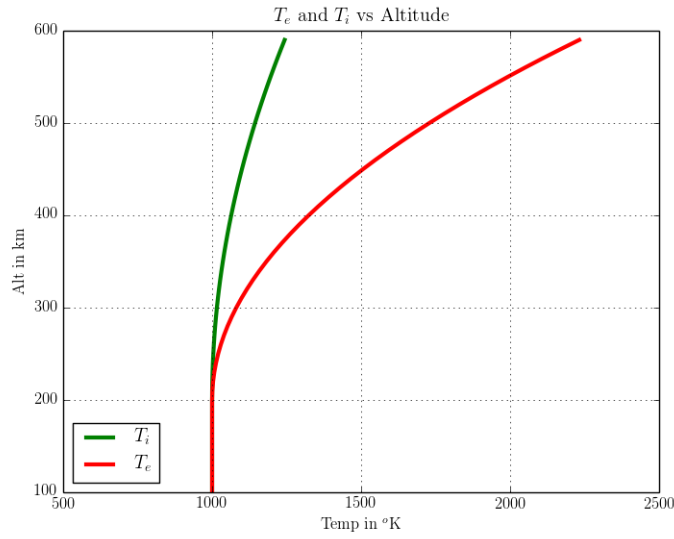**Figure 12.**   Stationary phantom along with both types of reconstructions.

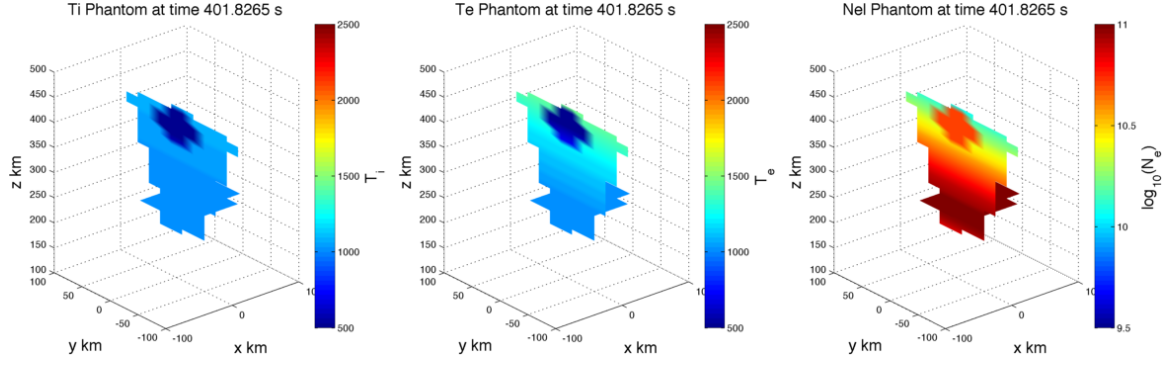**Figure 13.**   Ion & Electron Temperature vs. Height.
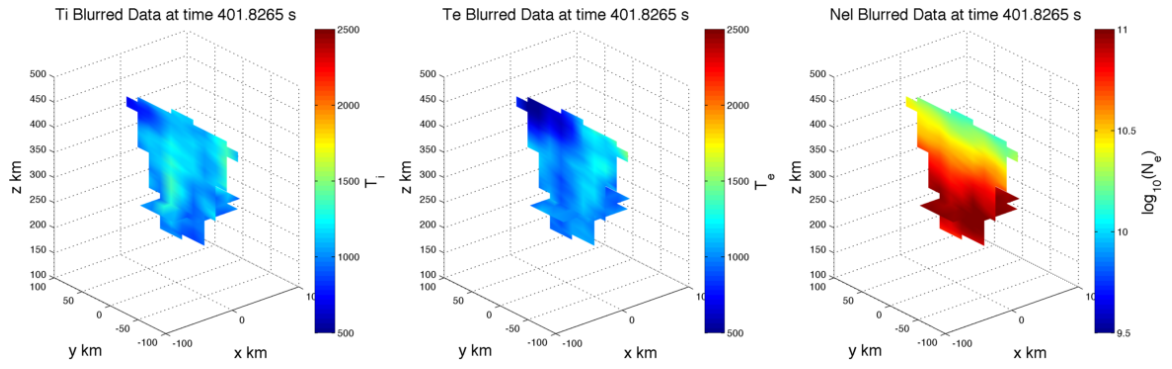
Figure 14. Phantom of Parameters.

Figure 15. Interpolated Data after Full Fitting.